International Journal of Fatigue 163 (2022) 107072

Contents lists available at ScienceDirect

International Journal of Fatigue

journal homepage: www.elsevier.com/locate/ijfatigue

Analytical fatigue life formulation for notches informed by crystal plasticity

Farhan Ashraf [a], Andrea Cini [b], Gustavo M. Castelluccio [a,*]

[a] School of Aerospace, Transport and Manufacturing, Cranfield University, Bedfordshire MK43 0AL, UK
[b] Bioengineering and Aerospace Engineering, University Carlos III of Madrid, Avd. de la Universidad, 30, 28911, Leganes, Madrid, Spain

ARTICLE INFO

Keywords:
Small cracks
Crystal plasticity
Microstructure
Scribe marks
Micromechanical notches

ABSTRACT

Damage from small manufacturing defects often go unnoticed until fatigue cracks have grown beyond repairability. These cracks initiate at defects with dimensions on par with the microstructure length scale (e.g., 5–200 μm deep), which affects fatigue variability and renders most engineering prognosis methods inapplicable. This work develops a novel microstructure-sensitive formulation that reduces computational efforts by decoupling geometric and microstructural contributions to fatigue cracking. Crystal plasticity finite element models with and without geometry induced strain gradients were considered to assess the role of defects independently from the microstructure. The analysis results in a fatigue life analytical formulation whose parameters depend on the microstructure and defect morphology.

1. Introduction

Manufacturing and maintenance operations often result in relatively shallow defects (5–200 μm deep) also known as scribe marks, which promote fatigue crack nucleation under alternating service loads [1–4]. Although such defects can prove detrimental to structural integrity [4,5], they are often ignored due to the difficulties in making accurate remaining life estimations. Hence, advances in life prognosis for shallow defects (compared to the microstructural length scale) are valuable to improve component reliability and extend service life. This is particularly important for aerospace applications, where aircraft skin damage may go unnoticed until cracks have grown beyond reparability [1,4,5].

Several authors [5–7] have investigated the role of geometric discontinuities on fatigue crack nucleation and propagation. For example, Cini and Irving [1,8] characterized the nucleation of fatigue cracks in Al 2024 and pure Al cladding from shallow defects and found that the early fatigue crack growth depends on the notch size and shape. This behavior was attributed to the notch dimensions being comparable to the microstructure length scale (e.g., grain size). Indeed, when the volume of highly strained material ahead of a defect (i.e., process zone) is comparable to the microstructural dimensions, the local anisotropy and heterogeneity control fatigue damage [9]. Under these conditions, the applicability of traditional far-field fracture mechanics approaches becomes questionable given that the similitude assumption breaks down [10,11]. Even if traditional approaches were applicable, they do not generally consider or predict the variability of the fatigue process.

Prof. McDowell pioneered in microstructure-sensitive fatigue modelling by realizing the limitations of traditional fracture mechanics and developing approaches to quantify intrinsic fatigue variability. For example, Bennett and McDowell [12] extended the work by Fatemi and Socie [13] and proposed a Fatigue Indicator Parameter (FIP), which correlates with the crack tip displacement on a critical slip plane. In parallel, other researchers [14–17] considered FIPs based on stress, strain, or critical energy to estimate short crack fatigue driving forces. Hochhalter et al. [18] and Rovinelli et al. [19] independently compared multiple FIP formulations to show that they carry failure information with equivalent uncertainty levels. Hence, these FIPs are roughly equivalent to explain much of the fatigue phenomena and serve as computationally efficient subrogates of the damage driving forces.

McDowell and collaborators further demonstrated that crystal plasticity computational models along with nonlocal Fatemi-Socie FIPs [20–23] can quantify fatigue crack initiation at a microstructural scale [24–26]. Hence, crystal plasticity is a valuable tool to predict crack initiation and early propagation from scribe marks by characterizing both microstructural variability and geometrical discontinuity effects on crack evolution [1,8]. However, the introduction of strain concentrators results in large computational models that quickly become numerically expensive [27,28], making their engineering application prohibitive. Hence, this work extends prior efforts by decoupling geometry and microstructure effects on fatigue crack nucleation to develop an engineering approach with a lower computational burden. Microstructural variability quantified with crystal plasticity simulations is modulated by

* Corresponding author.
E-mail address: castellg@cranfield.ac.uk (G.M. Castelluccio).

https://doi.org/10.1016/j.ijfatigue.2022.107072
Received 15 February 2022; Received in revised form 6 May 2022; Accepted 6 June 2022
Available online 9 June 2022

Table 1
Crystal plasticity parameters corresponding to pure Al.

μ	25.6 GPa	v_G	$5x10^{11}$ s^{-1}
b	$2.86x10^{-10}$ m	K_{struc}	2.5
F_o	0.8 eV	α_{LE}	1
s_o	12 Mpa	A_{ii}	0.1
f_{inf}	0.1	ρ^{α}	1×10^{9}
f_o	0.45	y_e	3.5 nm
g_p	0.0015	y_s	50 nm
G_{PSB}	1×10^{-2}	V_{cs}	$1000b^3$
G_M	1×10^{-4}		

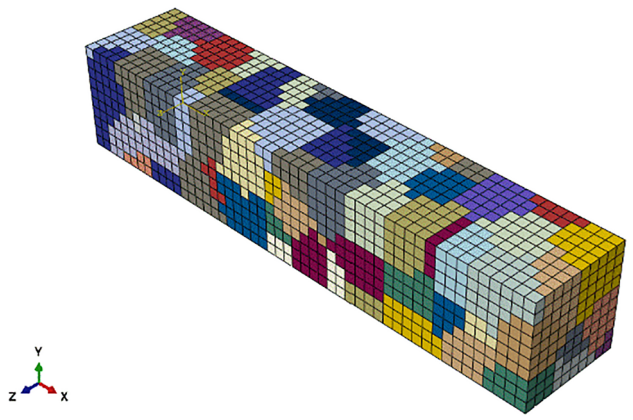

Fig. 1. Finite element mesh for a RVE of 200 μm × 200 μm × 1000 μm. Colors correspond to different crystallographic orientations.

the decay of the maximum shear strain computed radially from a notch with isotropic elastic–plastic simulation [29]. The result is a novel analytical formulation suitable for describing the early fatigue life from scribe marks and microstructural-size defects. The comparison with experimental data from scribe marks demonstrates that the novel approach has good predictive power for the fatigue life and its variability at a reduced computational cost.

2. Crystal plasticity modelling

This work considers a physics-based crystal plasticity model [20,30] calibrated for aluminium. The slip rate along α^{th} slip system follows the thermally activated flow rule,

$$\dot{\gamma}^{\alpha} = \dot{\gamma}_0^{\alpha}\exp\left[-\frac{F_0}{k_B T}\left\{1-\left(\frac{\langle|\tau^{\alpha}-B^{\alpha}|-S^{\alpha}\rangle}{s_0^t\frac{\mu}{\mu_0}}\right)^{p}\right\}^{q}\right] sgn(\tau^{\alpha}-B^{\alpha}) \tag{1}$$

in which $\dot{\gamma}_0^{\alpha}$ is the average shearing rate between the obstacles, k_B is the Boltzmann constant, F_o is the glide activation energy, s_o is the thermal stress at 0 K, and p and q are the profile parameters. Also, μ and μ_0 are the shear modulus at T and 0 K while the average shearing rate ($\dot{\gamma}_0^{\alpha}$) follows,

$$\dot{\gamma}_0^{\alpha} = \rho^{\alpha} b l v_G \tag{2}$$

in which v_G is the attempt frequency, ρ^{α} is the density of mobile dislocations, b is the Burgers vector and l is a mean free path of dislocation in between the obstacle bypass events and computed following the characteristics of dislocation substructure as $\eta \times d_{struc}$. The parameter η represents the dislocation substructure aspect ratio: $\eta_{veins} = 50$, $\eta_{PSB} = 15$, $\eta_{lab} = 2$, and $\eta_{cell} = 1$ [20].

The effective shear stress (τ_{eff}^{α}) i.e., $|\tau^{\alpha} - B^{\alpha}| - S^{\alpha}$ drives dislocation glide and depends on the local resolved shear stress (τ^{α}), the athermal stress (S^{α}), and intragranular back stress (B^{α}). The athermal stress depends on the stress required to bow-out dislocations and the dislocation self-interaction, i.e.,

$$S^{\alpha} = \alpha_{LE}\frac{\mu b}{(1-f_w)d_{struc}} + \mu b\sqrt{A_{ii}\rho^{\alpha}} \tag{3}$$

in which α_{LE} is the dislocation line energy coefficient, A_{ii} is the self-interaction coefficient. The parameter d_{struc} is the adjacent wall spacing and follows the similitude relation [31],

$$d_{struc} = K_{struct}\frac{\mu\, b}{\tau} \tag{4}$$

where K_{struct} is similitude coefficient. In Equation (1), we considered intragranular back stress (B^{α}) following Castelluccio and McDowell [20] as,

$$\dot{B}^{\alpha} = \frac{f_w}{1-f_w}\,\frac{2\mu(1-2S_{1212})}{1+4S_{1212}\mu f_{Hill}^{S}}\dot{\gamma}^{\alpha} \tag{5}$$

where, f_w is the wall volume fraction, f_{Hill}^{S} is the instantaneous macroscopic plastic deformation tangent. The Eshelby tensor component (S_{1212}) for a prolate spheroid coordinate system follows [32],

$$S_{1212} = \frac{\pi\eta^2 + (\eta^2 - 1.75 - 2\nu_p\eta^2 + 2\nu_p)C_{12}}{8\pi(1-\nu_p)(\eta^2-1)}, \tag{6}$$

$$C_{12} = \frac{2\pi\eta(\eta\sqrt{(\eta^2-1)} - \cosh^{-1}\eta)}{\sqrt[3]{(\eta^2-1)}} \tag{7}$$

and,

$$\nu_p = \frac{\nu + \frac{2}{3}\mu(1+\nu)f_{Hill}^{S}}{1+\frac{4}{3}\mu(1+\nu)f_{Hill}^{S}} \tag{8}$$

and finally, the density of mobile dislocations (ρ^{α}) follows,

$$\dot{\rho}_m^{s\alpha} = \frac{k_{multi}}{b l_{struc}}|\dot{\gamma}^{\alpha}| - \frac{2y_s^{edge}}{b}\rho_m^{s\alpha}|\dot{\gamma}^{\alpha}| - \frac{2\pi}{\mu b d_{struc}}|\dot{\tau}_{eff}|\,|^{unload} + v_G\frac{d_{struc}}{d_0}\left(\phi_{cs}\sum_{\xi=1(\xi\neq\alpha)}^{N}\rho_m^{s\xi}e^{\left(-V_{CS}^{\alpha}\frac{\frac{\mu b}{4\pi y_s^{screw}}-|\tau^{\alpha}-B^{\alpha}|}{k_B T}\right)} - (1-\phi)\sum_{\xi=1(\xi\neq\alpha)}^{N}\rho_m^{s\alpha}e^{\left(-V_{CS}^{\xi}\frac{\frac{\mu b}{4\pi y_s^{screw}}-\left|\tau^{\xi}-B^{\xi}\right|}{k_B T}\right)}\right) \tag{9}$$

Here, k_{multi} determines the production of dislocations, $V_{CS}^{0} = 1000b^3$ corresponds to the cross-slip activation volume[33], y_s^{edge} and y_s^{screw} are the annihilation distances for edge and screw dislocations respectively, and ϕ is the cross-slip efficiency. Further details of the model can be found in [20] whereas model input parameters, material, and physical constants are shown in Table 1.

The crystal plasticity model was implemented in Abaqus through a

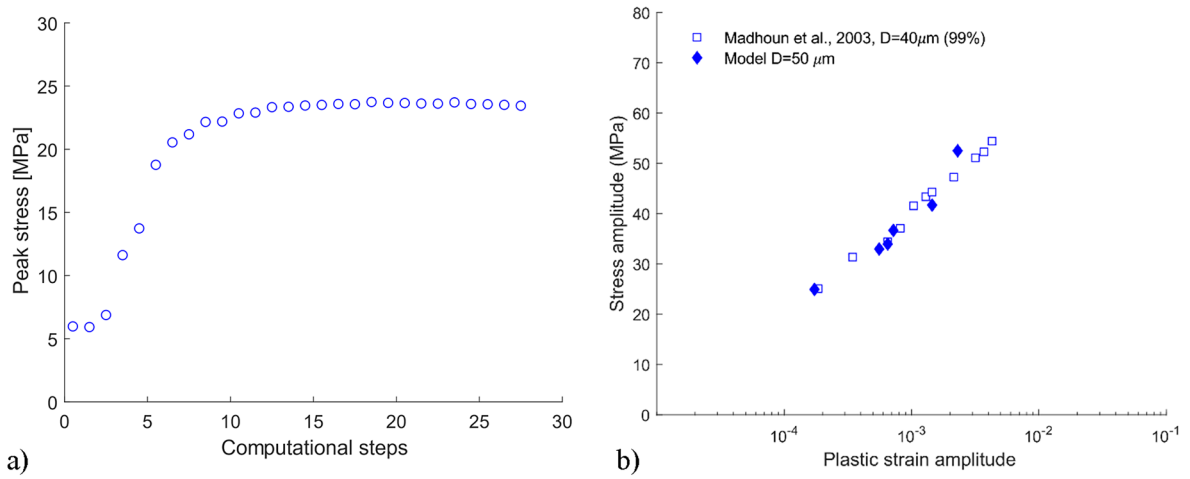

Fig. 2. a) Evolution of cyclic peak stress, and b) Maximum FIP_{FS} across all grains with computational steps for pure Al under $\Delta\epsilon/2 = 0.05\%, 0.1\%\ s^{-1}$, and $R_\epsilon = -1$ b) Comparison between model and experiment for the cyclic stress–strain response of Al polycrystal [39].

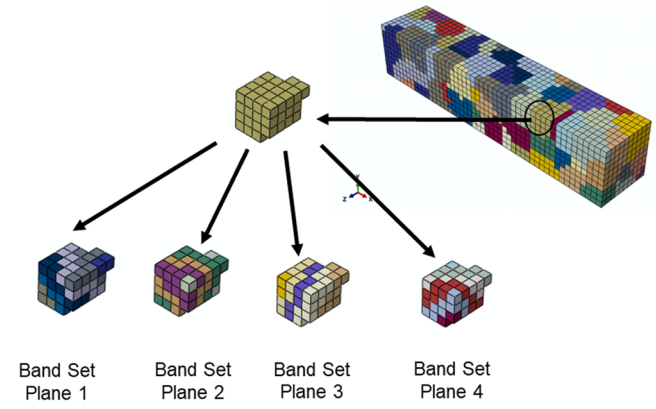

Fig. 3. Illustration of slip bands in one grain. As an example, four sets of slip bands along the slip planes perpendicular to FCC slip normal direction are shown in one grain.

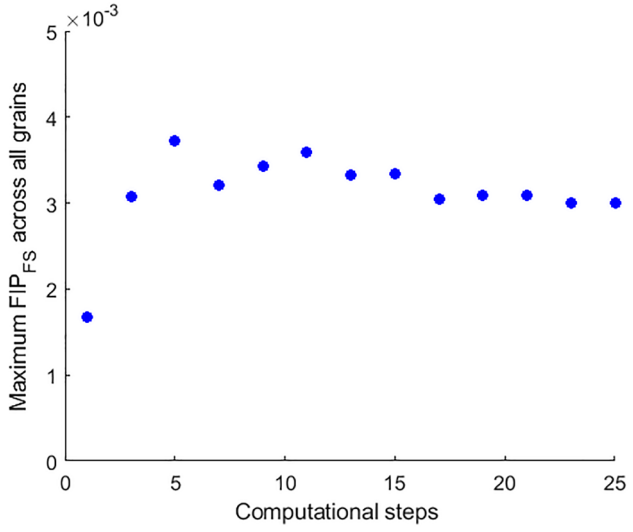

Fig. 4. Maximum FIP_{FS} across all grains with computational steps for pure Al under $\Delta\epsilon/2 = 0.05\%, 0.1\%\ s^{-1}$, and $R_\epsilon = -1$. These results demonstrates that the maximum FIPs also saturates at about after 8 loading cycles (16 Abaqus steps).

user material (UMAT) subroutine. The constitutive model was evaluated using regular geometry with 5000 C3D8R brick elements and 122 randomly oriented grains (average grain size ~ 80 μm) shown in Fig. 1. The microstructure, corresponding to the equiaxed randomly oriented grain structure observed in the pure aluminium cladding [34], was recreated with Dream3D [35] and an in-house Matlab script. A synthetic representation of the microstructure requires around one hundred grains [36,37] to approximate the constitutive response of a Representative Volume Element (RVE) [38]. Note that an RVE for fatigue crack nucleation requires a much larger number of grains and mesh refinement.

Fig. 2(a) presents the homogenized mechanical response of the model as a function of the number of Abaqus steps (one full loading cycles corresponds to two steps). The results demonstrate that the peak stress converges to a stable value after twelve computational cycles. Fig. 2(b) further validates the cyclic stress–strain curves by comparing the model and experimental results for polycrystal Al [39]. Each modeling data point (diamond) corresponds to the stress level at twelve computational cycles.

3. Crystallographic FIPs

3.1. Non-local FIPs

We define the fatigue driving force as the crystallographic Fatemi-Socie FIP (FIP^{α}_{FS}) proposed by Castelluccio and McDowell [38], but noting that our conclusions are likely applicable to other FIP formulations [19]. Then, we compute the FIP^{α}_{FS} for each element by,

$$FIP^{\alpha}_{FS} = \frac{1}{2}\Delta\gamma^{\alpha}|_{cyc}\left[1 + k\frac{\sigma^{\alpha}_{n}}{\sigma_{y}}\right], \tag{10}$$

where $\Delta\gamma^{\alpha}$ corresponds to the cyclic plastic shear strain range in slip plane α, σ^{α}_{n} is the peak stress normal to the slip plane α, σ_y is the cyclic yield strength, and $k = 1$ is a material constant normally ranging between 0.5 and 1 [13].

Following the approach proposed by Castelluccio and McDowell [38], the algorithm uses Equations (10) to compute FIP^{α}_{FS} at each element upon reaching peak stress stabilization (12th loading cycle or 24th computational step). Next, FIP^{α}_{FS} are averaged over the volume of crystallographic slip bands, which serve as physics-based normalization domains to mitigate mesh sensitivity. The bands are one-element thick and perpendicular to each slip plane normal direction, as shown in Fig. 3. Furthermore, each grain can be fully reconstructed by the band set corresponding to each slip normal (Fig. 3). Appendix A presents in

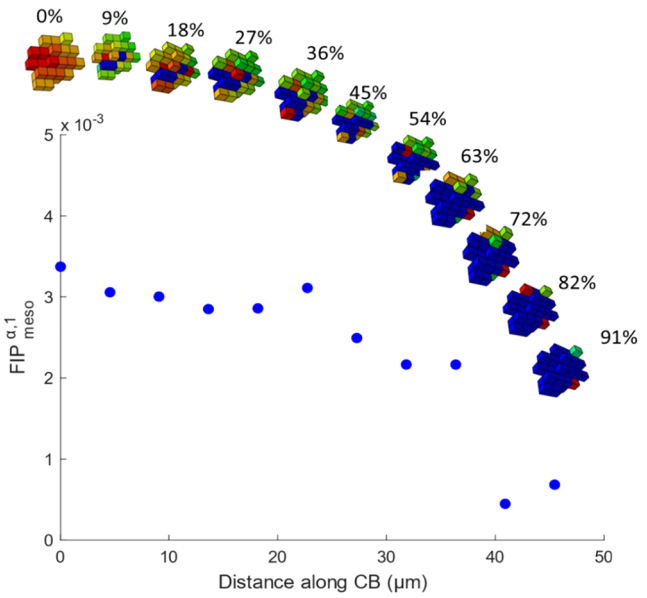

Fig. 5. FIP_{FS}^{Meso} variation as crack extends inside a CB. The first image (top left corner) corresponds to FIP_{FS}^{Meso} computed for the entire CB (0% crack extension). The increasing blue color in subsequent images shows elastically degraded elements in CB, and the blue dots under each image represents averaged FIP_{FS}^{Meso} in the remaining elements of CB. (For interpretation of the references to color in this figure legend, the reader is referred to the web version of this article.). (For interpretation of the references to color in this figure legend, the reader is referred to the web version of this article.)

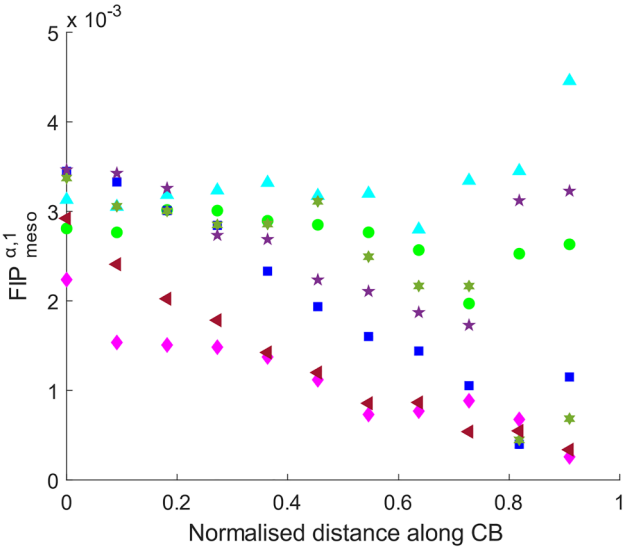

Fig. 6. FIP_{meso} variation as the crack extends along a CB. Each curve corresponds to a different simulation with a different microstructure realization. The distance on the x-axis is normalized by the maximum distance along CB.

detail the procedure for recreating slip bands sets on each grain.

The FIP_{FS}^{α} averaged along crystallographic slip bands is further normalized such that.

$$FIP_{FS}^{Meso} = \frac{d_{gr}}{d_{gr}^{ref}} \frac{\sum_1^n FIP_{FS}^{\alpha}}{n} \tag{11}$$

in which d_{gr}^{ref} is the reference grain size and d_{gr} represents the band size as computed by,

$$d_{gr} = l_{el}\sqrt{n_{el}}. \tag{12}$$

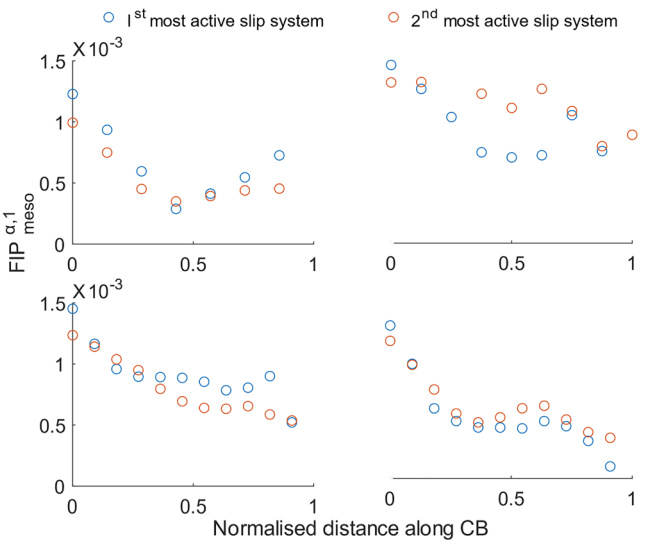

Fig. 7. Variation of FIP_{meso} in CB along 1st and 2nd most active slip systems as crack extends for four random realizations. The distance on the x-axis is normalized by the maximum distance along CB.

where, l_{el} is the size of the element and n_{el} is the number of uncracked elements in the band. This normalization is supported by the size dependence of irreversible slip proposed by Risbet and Feaugas [40]. Finally, the band with the highest FIP_{FS}^{Meso} is considered to be the slip band initiating a fatigue crack and is referred to as the Cracked Band (CB). Fig. 4 further illustrates that the maximum FIP_{FS}^{Meso} among all grains (i.e., the highest FIP_{FS}^{α} average among all bands) converges after 16 computational steps (8 full loading cycles), which demonstrates that FIP_{FS}^{Meso} is well suited for microstructure-sensitive fatigue prognosis.

3.2. Intragranular FIP evolution

The average of FIP_{FS}^{Meso} along an entire band is representative of the fatigue driving forces of an uncracked slip band. Hence, partially cracked bands are simulated by degrading all components of the elastic stiffness matrix [38] for the elements on the band with the highest FIP_{FS}^{α}. This calculation proceeds every two computational cycles, after which the FIP_{FS}^{Meso} is averaged on the remaining uncracked elements in the band. Fig. 5 exemplifies the evolution of FIP_{FS}^{Meso} as the crack grows through the grain, cracking 9% of the elements with the highest FIP_{FS}^{α} every two computational cycles. The FIP_{FS}^{Meso} reduces as the crack grows in the band, which agrees with the modelling of nickel based superalloys [38], bridge steel [41], and also experimental findings [42]. Fig. 6 further shows the evolution of the FIP_{FS}^{Meso} with the normalized crack length for various grains in Fig. 1. Evidently, the intragranular nature of FIP_{FS}^{Meso} depends on the interaction of complex microstructural attributes such as crystallographic orientation, neighbouring grains, and number of active slip planes.

To further explore the role of multiple slip, Fig. 7 presents the FIP_{FS}^{Meso} for the first and second most active slip system, computed for the same CBs. The results demonstrate that in a partially cracked band, the activation of the second most active slip plane prior to cracking, can exceed that of the primary plane. Hence, Equation (11) is amenable to single slip configurations and less applicable to Al, given its low activation energy and consequent tendency for multiple slip.

To account for multiple slip and crystallographic FIPs, we propose a novel strategy that computes the net driving force ($\overrightarrow{FIP}_{meso}$) as the vector sum of FIP_{meso} along the directions of the three most active slip planes slip directions ($\boldsymbol{n}_{i,j,k}$), i.e.,

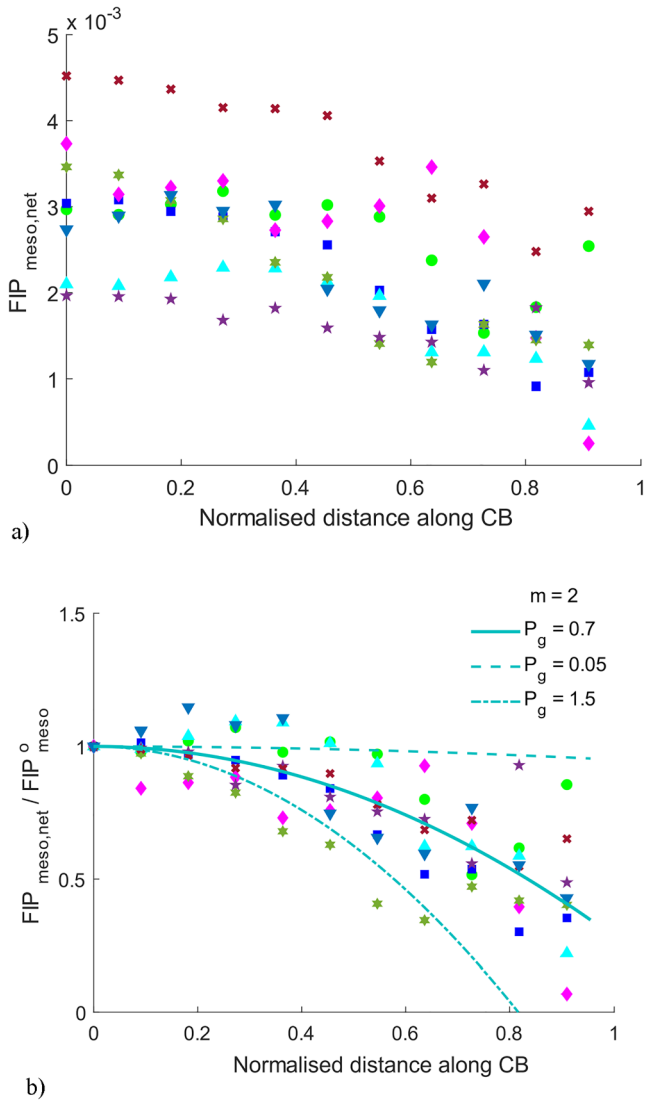

Fig. 8. a) Multiple realizations for the $\overrightarrow{FIP}_{meso}$ as a function of crack extension within a single grain. The distance on x-axis is normalized by the maximum distance along CB until fully cracked. b) Normalized $\overrightarrow{FIP}_{meso}$ (Equation (14)) as a function of the transgranular crack extension. The distance on x-axis is normalized by the maximum distance along CB until fully cracked.

$$\overrightarrow{FIP}_{meso} = \frac{1}{d_{gr}^{ref}}\left[d_{gr,i}FIP_{FS}^{MesoMAX}(i)\boldsymbol{n_i} + d_{gr,j}FIP_{FS}^{MesoMAX}(j)\boldsymbol{n_j} + d_{gr,k}FIP_{FS}^{MesoMAX}(k)\boldsymbol{n_k}\right]. \tag{13}$$

where, $FIP_{FS}^{MesoMAX}$, $FIP_{FS}^{Meso2ndMAX}$, and $FIP_{FS}^{Meso3rdMAX}$ are the FIPs along the 1st, 2nd, and 3rd most active slip planes averages on the band. Averaging along bands, as explained before, introduces a directional character and makes the $\overrightarrow{FIP}_{meso}$ a multiple slip crystallographic driving force. The $\overrightarrow{FIP}_{meso}$ is then be computed for each band, assuming that the driving force along the dominant cracking direction is assisted by multiple slip. This notion is supported by the experiments of Grosskreutz in Al single crystals [43], which showed that an initial dominant slip band is assisted by bursts of secondary slip plane activation.

Fig. 8 a) presents the results for the $\overrightarrow{FIP}_{meso}$ computed along CB from eight microstructural realizations while degrading the elastic stiffness incrementally after every two cycles until fully cracked. The magnitude of the $\overrightarrow{FIP}_{meso}$ decays as the crack progresses within the grain and the decrease is more pronounced than in Fig. 6. Fig. 8b) presents the same results normalized by the $\overrightarrow{FIP}_{meso}$ prior to any grain cracking ($\overrightarrow{FIP}^{0}_{meso}$). The normalized fatigue driving force can be parameterized as a function of crack length as suggested by Castelluccio and McDowell [38],

$$\left|\overrightarrow{FIP}_{meso,net}\right| = \left|\overrightarrow{FIP}_{meso}\right| / \left|\overrightarrow{FIP}^{0}_{meso}\right| = 1 - P_g\left(a_i/d_{gr}\right)^m \tag{14}$$

where a_i/d_{gr} corresponds to the crack length normalized by the slip band length and P_g and m are constants fit to the data in Fig. 8. Equation (14) can be further simplified by assuming $m = 2$ as initially proposed Castelluccio and McDowell [38]. In this case, Fig. 8 b) demonstrates that $m = 2$ and P_g in the range between 0 and 1.5 (Fig. 8) adequately describes the intragranular microstructural variability of the $\overrightarrow{FIP}_{meso}$, even in the context of multiple slip.

3.3. Crack initiation from defects

Next, we consider the evolution of FIPs starting from a 25 μm deep scribe marks with root radii of 5 μm, 25 μm and 50 μm [1], as shown in Fig. 9. U-notches were considered instead of the V-shaped traditionally used for scribe marks simulations [1,8] to simplify the mesh while obtaining the similar local stress and strain conditions [44]. The model conveys a notch with a local fine mesh covering a section five times greater than the notch with a minimum seed size of 2 μm. Periodic boundary conditions are applied along the Z-axis, which entails to a null sum of the displacement of the node on opposite front and back faces while all other faces are free to displace. A fully reversed ($R_\epsilon = -1$) strain amplitude of 5×10^{-5} was applied to the right-hand side of Fig. 9 along the X-axis. To reduce the computational effort, the crystal plasticity model is employed only around the notch root with a refined mesh. The remaining of the mesh employs an isotropic elasto-plastic model constructed with the piece-wise stress–strain curve obtained from homogenized crystal plasticity model results in Fig. 2.

The microstructure contains a total of 16 grains with an average grain diameter of 50 μm along the X-Y direction and 120 μm along the Z-direction; this elongated morphology of the microstructure resembles the cladding assessed by Cini et al. [1,8]. As explained earlier, slip bands are created along crystallographic planes and $\overrightarrow{FIP}_{meso}$ are computed for each of them.

Fig. 10 presents normalized $\overrightarrow{FIP}_{meso,net}$ computed from models with notches. Compared to the calculations from smooth models (Fig. 8(b)), the $\overrightarrow{FIP}_{meso,net}$ in Fig. 10 decays more rapidly due to the strain localization induced by the notch. These $\overrightarrow{FIP}_{meso,net}$ responses can also be parameterized by Equation (14), but running crystal plasticity models with notches to quantify m and P_g is significantly more computationally expensive and the results are only applicable to the specific notch geometry. On the contrary, the parameters m and P_g computed without notches Fig. 8(b) can be regarded as an intrinsic microstructure response.

4. Decoupling microstructure and geometry contribution to FIPs

To avoid crystal plasticity simulations that explicitly model notches, we seek a simpler engineering method that modulates the intrinsic microstructural variability from models without notches. Rovinelli et al. [19] showed that the FIP_{FS} and plastic shear strain range are similar in predicting fatigue damage. Hence, the decay of the maximum plastic shear strain (γ^{pl}_{max}) computed with homogenous isotropic elastic–plastic simulations radially from a notch is a cost-efficient candidate to represent the notch modulation of the microstructural variability.

To account for the directionality of crack initiation from notches, we quantify the γ^{pl}_{max} along a radial direction between 10 and 54 degrees away from the notch bisector in isotropic elastic–plastic models (Fig. 9).

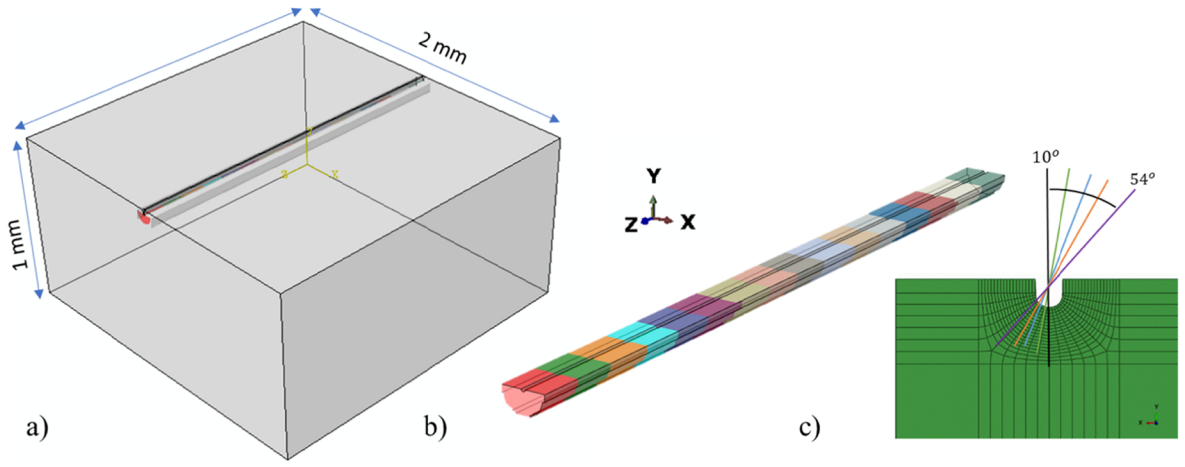

Fig. 9. a) Notched finite Element model. Grey volume was assigned the elasto-plastic model constructed with the piece-wise stress–strain curve. b) The coloured region contain grains around the notch and employ the crystal plasticity model. c) Directions along the notch root radii for evaluating the driving force gradient.

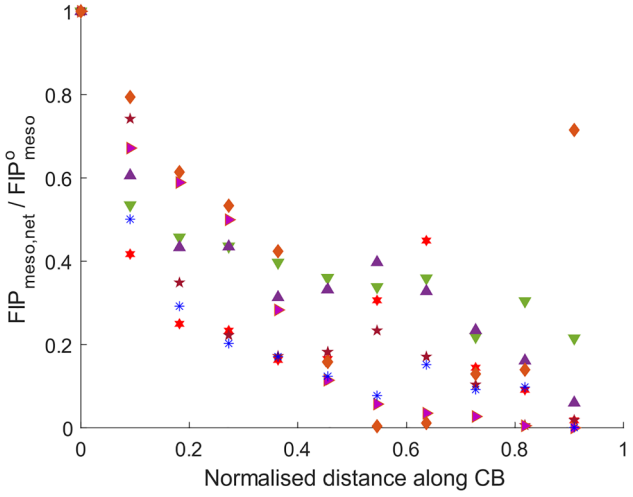

Fig. 10. Effect of microstructure and geometric gradient on normalized $FIP_{meso,net}$ with crack extension in CB at nominal strain amplitude of 5×10^{-5}. The ordinate is normalized by max $FIP_{meso,net}$ at 0% crack length. The distance on x-axis is normalized by the maximum distance along CB. Each color and marker correspond to a realization with a different microstructure. Each point represents the crack extension by deleting 9% element every two-cycle after nucleation evaluation i.e., 12 computational cycles.

Fig. 11 presents the normalized γ^{pl}_{max} as a function of the normalized radial distance from the notch along different angles for two notch radii (5 μm and 50 μm). On the Y-axis, the maximum plastic shear strain is normalized by the maximum plastic shear strain at notch root and the distance is normalized by the average grain size used for microstructural gradient i.e., 50 μm. The relation between normalized γ^{pl}_{max} and normalized radial distance was described by the inverse of second-order Taylor approximation,

$$\gamma^{pl}_{max}/\gamma^{pl}_{\max,notchtip} = 1/\left(1 + k_1 x + k_2 x^2\right) \tag{15}$$

Where, k_1 and k_2 are the fitting parameters for each notch radius, as shown in Fig. 11. Equation (15) corresponds to the geometry-induced shear strain decay. Second-order polynomial functions approximated the normalized γ^{pl}_{max} distributions along different direction as shown in Fig. 11.

The superposition of the microstructure and notch effects can be reconstructed by multiplying the microstructural decay in Equation (14) and the geometry-induced shear strain decay in Equation (15), i.e,

$$\overrightarrow{FIP}_{meso}/\overrightarrow{FIP}^{0}_{meso} = 1 - P_g\left(a_i/d_{gr}\right)^m \bullet \frac{1}{1 + k_1\left(a_i/d_{gr}\right) + k_2\left(a_i/d_{gr}\right)^2} \tag{16}$$

The value of this formulation is that the computational cost is controlled by the quantification of P_g and m using crystal plasticity simulations without notches (Fig. 8(b)). To validate the novel approach, Fig. 12 compares the simulations that explicitly represent the notch and the surrogate approach of Equation (16). The variability in the surrogate model is controlled by P_g, m, and the propagation angle along the radial directions (directionality of crack initiation from notches). By controlling these parameters in surrogate models, the variability of expensive models can be reproduced with less computational effort. Fig. 12 demonstrates that the novel surrogate model has similar trends and variability as the brute force model for the same number of microstructural realizations. In terms of computation effort, simulations with explicit notches were completed in an average of 80 h, whereas the suggested simplified methods took only 2 h.

5. Life estimation results

We now proceed to quantify the fatigue life of early transgranular Stage I cracks growing radially from notches. Since the strain localization at the notch root accelerates the nucleation of cracks, we assume that fatigue life is controlled by propagation in the microstructurally small crack regime [45]. Following the work by McDowell and co-authors [30,46,47], the crack growth rate can be related to the FIP such that,

$$\frac{da}{dN} = \varnothing\,\langle \frac{d_{gr}}{d^{ref}_{gr}} FIP_{meso,\ net}(j,\alpha) - \Delta CTD_{th}\rangle \tag{17}$$

where $\varnothing$ corresponds to the mechanical irreversibility and strongly depends on the environment. We consider $\varnothing = 0.012$ [25] for transgranular crack growth whereas $d^{ref}_{gr} = 40\mu m$, as per the calibration by Castelluccio and McDowell [42]. The ΔCTD_{th} serves as threshold below which there is no crack growth and its value is approximated by the Burgers vector for aluminium ($b \approx 2.8 \times 10^{-10} m$). By combining Equations (16) and (17) we obtain,

$$\frac{da}{dN} = \varnothing\,\langle \frac{d_{gr}}{40\mu m} \overrightarrow{FIP}^{0}_{meso} \left(\frac{1 - P_g\left(a_i/d_{gr}\right)^m}{1 + k_1\left(a_i/d_{gr}\right) + k_2\left(a_i/d_{gr}\right)^2} \right) - \Delta CTD_{th}\rangle, \tag{18}$$

which describes the crack growth rate at a radial distance a_i from a notch. The microstructural variability is controlled by P_g and m as computed from the RVE crystal plasticity models, while the notch

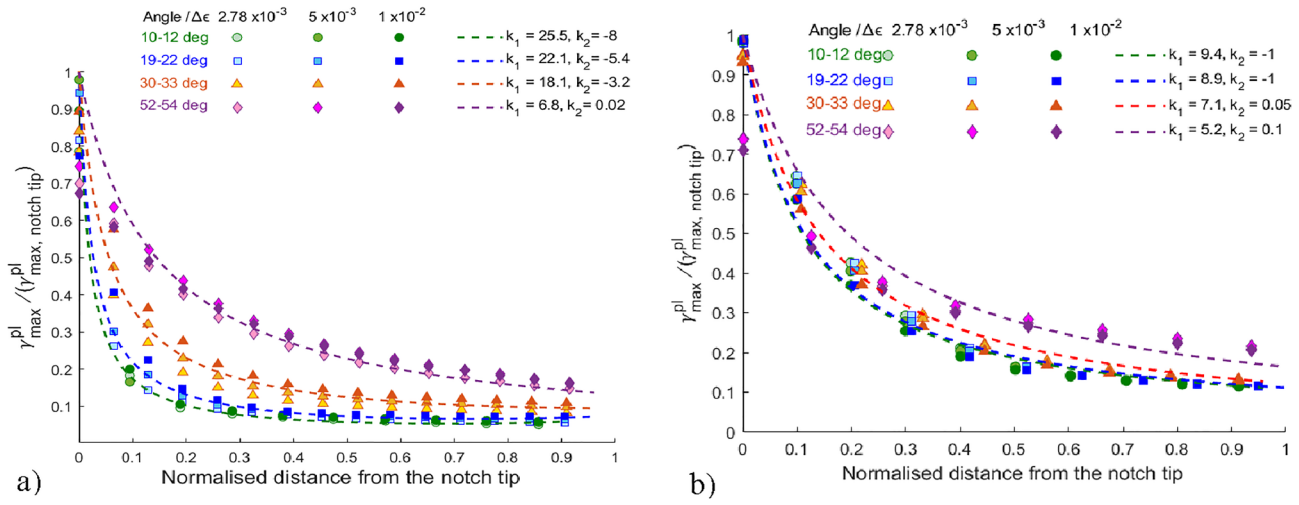

Fig. 11. The gradient of normalized γ^{pl}_{max} away from the notch tip for radius a) 5 μm and b) 50 μm at different nominal strains. The γ^{pl}_{max} was normalized with the maximum γ^{pl}_{max} at the notch tip. The distance is normalized by the average grain size used for microstructural gradient i.e., 50 μm.

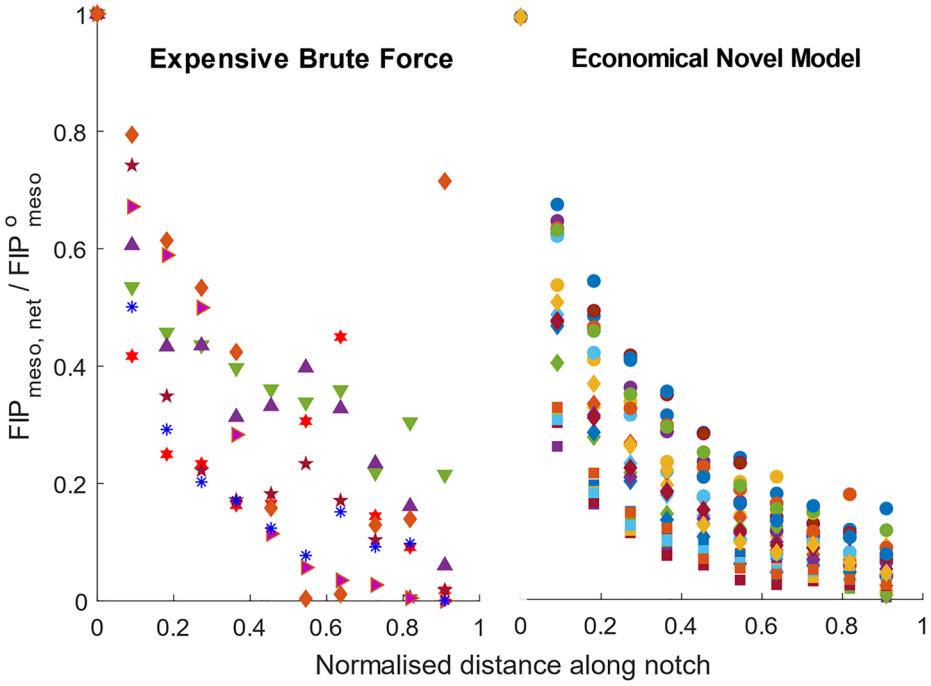

Fig. 12. Comparison between simultaneous estimation and combination of gradients at a fully reversed strain amplitude of $5x10^{-5}$. $FIP_{meso,net}$ is normalized by FIP_o, which is a FIP_{meso} at 0% crack extension. The normalization distance on the x-axis corresponds to the average grain size used for microstructural gradient i.e., 50 μm. Each color in Figure (left) represents different simulation results with different microstructure and morphological properties. Each marker in Figure (right) represents independently coupled FIP with both microstructure and geometric gradient. The results for the surrogate model (right) correspond to k_1 and k_2 at 10–12, 30–33 and 52–54 degrees.

morphology regulates k_1 and k_2 as computed by isotropic elasto-plastic models.

By defining.

$$c_1 = \frac{d_{gr}}{40}\overline{FIP}^{0}_{meso} - \Delta CTD_{th} \tag{19}$$

and.

$$c_2 = P_g \frac{d_{gr}}{40}\overline{FIP}^{0}_{meso} \tag{20}$$

to integrate Equation (18) to compute the number of cycles requires to extend the crack by distance of a_i along the i^{th} band (N_{extend}).

$$N_{extend} = \int_o^{a_i} \frac{1}{\emptyset} \left\langle \frac{1}{c_1 - c_2\left({}^{a_i}/_{d_{gr}}\right)^m} + \frac{k_1\left({}^{a_i}/_{d_{gr}}\right)}{c_1 - c_2\left({}^{a_i}/_{d_{gr}}\right)^m} + \frac{k_2\left({}^{a_i}/_{d_{gr}}\right)^2}{c_1 - c_2\left({}^{a_i}/_{d_{gr}}\right)^m} \right\rangle da_i \tag{21}$$

Microstructure gradient — Geometric gradient

The first term in Equation (21) corresponds to the microstructural gradient proposed by Castelluccio and McDowell [38], while the linear and quadratic terms represent the contribution from the geometric gradient approximated by a second order Taylor expansion. For strains ranges above 10^{-4} (most common case at the notch root in service structures), numerical calculations have shown (see Appendix B) that the $\overrightarrow{FIP}^0_{meso}$ is significantly larger than ΔCTD_{th}. Hence, by neglecting the term ΔCTD_{th} and assuming $m = 2$, we can perform an analytical integration to obtain,

$$N_{extend} = \frac{1}{\emptyset}\left\langle \frac{d_{gr}}{\sqrt{c_1 c_2}} tanh^{-1}\left(\frac{a_i}{d_{gr}}\sqrt{\frac{c_2}{c_1}}\right) - k_1 \frac{d_{gr} ln(c_1 {d_{gr}}^2 - {a_i}^2 c_2)}{2c_2} + k_2 \frac{d_{gr}\sqrt{c_1} tanh^{-1}\left(\frac{a_i}{d_{gr}}\sqrt{\frac{c_2}{c_1}}\right) - a_i\sqrt{c_2}}{\sqrt[3]{c_2}} \right\rangle, \tag{22}$$

Microstructure gradient — Geometric gradient

which corresponds to a closed-form solution that quantifies the fatigue life to extend a radial crack in a grain, considering microstructural and geometry effect. Note that we could consider higher terms for the Taylor approximation for the maximum plastic shear strain away from the notch (Equation (15)). However, any improvement on these calculations would have marginal impact on the results given that the error is significantly smaller than the intrinsic microstructural variability (both in terms of driving forces and cracking angles).

The shortest expected life for a crack of length a_i arises from the lowest P_g computed with crystal plasticity simulations without notches and the highest k_1 and k_2 computed from elasto-plastic simulations. Similarly, the variability of life proceeds from considering the ranges of P_g, k_1, and k_2 computed in both models. The calculation in Equation (21) also requires the estimation of $\overrightarrow{FIP}^0_{meso}$ (see Equations (19) and (20)), which is a priori unknown unless crystal plasticity models with notches are performed. We propose an alternative computational efficient engineering approach that upscales $\overrightarrow{FIP}^0_{meso}$ following,

$$\overrightarrow{FIP}^0_{meso}\Big|_{\Delta\epsilon} = \frac{\Delta\epsilon}{\Delta\epsilon_{ref}} \overrightarrow{FIP}^{Ref}_{meso} \tag{23}$$

in which $\Delta\epsilon$ corresponds to the total strain range computed at the root of the isotropic notch model, $\Delta\epsilon_{ref} = 1 \times 10^{-3}$ is a constant reference total strain range applied to RVEs, and the parameter $\overrightarrow{FIP}^{Ref}_{meso}$ is the maximum $\overrightarrow{FIP}^0_{meso}$ computed from RVE simulations with an applied strain range of $\Delta\epsilon_{ref}$.

To validate Equation (23), multiple microstructural realizations of the RVE were simulated using crystal plasticity and total strain amplitudes between $10^{-3} - 10^{-2}$. For each simulation, the maximum $\overrightarrow{FIP}^0_{meso}$ from each grain were compiled to inform $\overrightarrow{FIP}^{Ref}_{meso}$. The results in Fig. 13

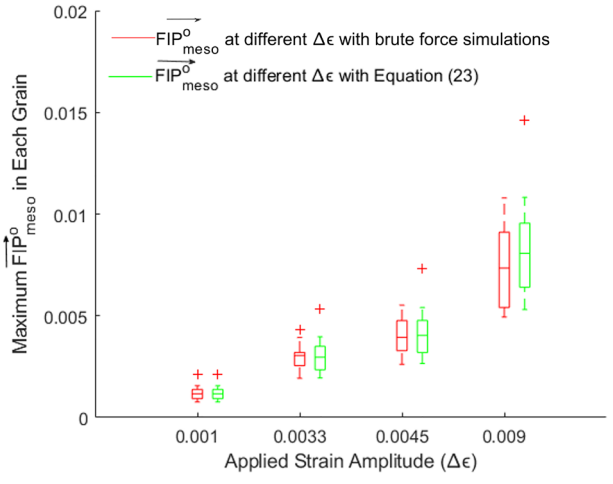

Fig. 13. Comparison of the maximum normalized FIP_{meso} across all grains with one microstructure realization from the calibrated and explicit notch model. The lower and upper quartiles correspond to the bottom and top of the boxes, respectively, and the medium quartile corresponds to the line near the middle of the box. A cross corresponds to outliers.

Table 2
γ_{pl}^{max} at the notch root for notches with different radii and the same depth i.e., 25 μm.

Notch radius	5 μm	25 μm	50 μm
γ_{pl}^{max}	1.4×10^{-1}	1.44×10^{-1}	8.6×10^{-2}
$\Delta\epsilon$	7.02×10^{-2}	7.2×10^{-2}	4.3×10^{-2}

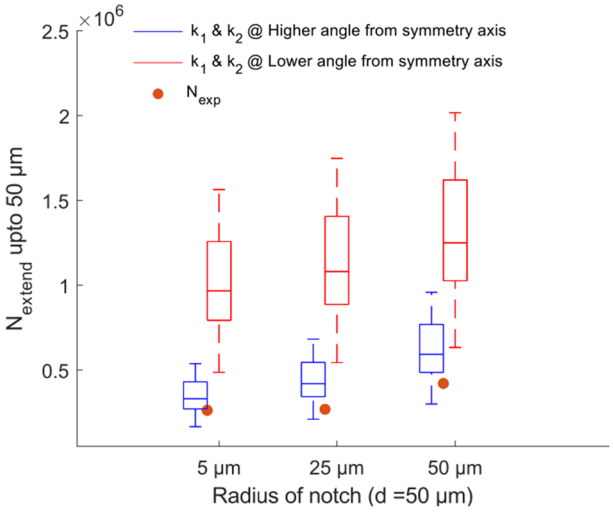

Fig. 14. Comparison of the number of cycles to extend the crack up to 50 μm between model and experiment [34]. The boxplot corresponds to the computational variability. The minimum predicted lives are in agreement with the experiments and capture notch size effects.

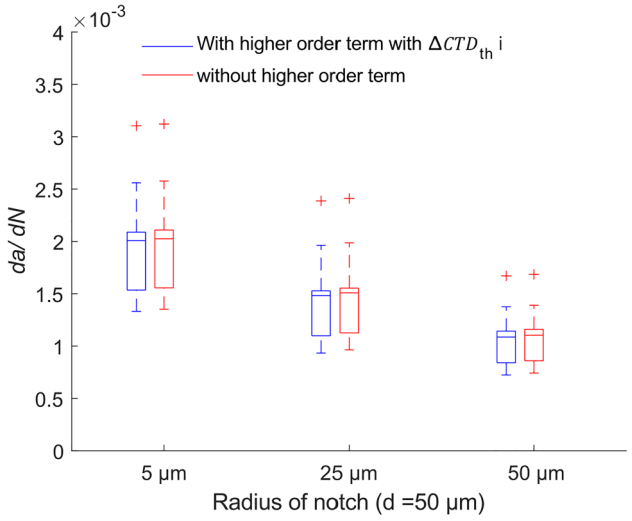

Fig. 16. Estimation of uncertainty with and without higher-order terms in Equation (18). The positive sign represents outliers.

demonstrate that the distributions of the $\overrightarrow{FIP}^{0}_{meso}$ computed with explicit notches (red) or Equation (23) (green).

Finally, we further validate our methodology by comparing the initiation lives calculated by Equation (22) with experimental data from Ref [1,34]. Three notch geometries with different root radii (5 µm, 25 µm and 50 µm), similar to those mentioned in Section 4, in pure aluminium cladding are considered. Experimental evidence [1,34] shows notch sensitivity in the microstructural small crack regime for 25–185 µm deep notch within pure Al cladding. The $\Delta\epsilon$ is estimated for different notch geometries using experimental loading conditions [34] as shown in Table 2.

The results in Fig. 14 compare the number of cycles to reach 50 μm in 20 microstructural realizations with the dominant crack found in experiments [1,8]. The variability of N_{extend} corresponds to the life required for a crack to reach 50 μm radially from the notch along 10 or 50 degrees from the notch bisector. The mechanical irreversibility is adjusted to match lowest N_{extend} for the 5 μm notch, and the simulations automatically reproduced the notch effect for other size without any special provision. In addition, the experiments showed multiple shorter cracks and uncracked areas, which correlates with the variability on simulations. Further work could explore multiscale experimental validation of Equation (22), including various loading conditions.

6. Discussion

Modeling fatigue damage variability is a critical aspect of probabilistic reliability assessments, which can be performed with microstructure-sensitive computational models. However, these models are computationally too intensive for industrial applications and require simpler surrogate models. This work introduced a novel analytical approach that combines geometric and microstructural strain gradients independently to predict transgranular fatigue life away from a notch. Crystal plasticity simulations of RVEs, which can be accelerated with Fast Fourier Transform methods, [48] are instrumental to quantify the parameters characteristic of the microstructural FIP evolution (P_g and m). These parameters are intrinsic to the microstructure and were combined with elastic–plastic models to evaluate the microstructure-induced fatigue variability from notch. As a result, the model can estimate efficiently the initiation fatigue lives from notches considering microstructure variability to evaluate durability requirements.

Other damage tolerant approaches, such as the theory of critical distances [8], can predict initiation life from scribe marks but they rely on phenomenological formulations that required extensive experimental testing. These theories depend on a characteristic length function of the load amplitudes, material and other testing to calculate equivalent elastic stresses able to correlate initiation lives [8]. Despite their success in predicting initiation lives from scribe marks, physical evidence is still needed to rationalise the correlation between the equivalent elastic critical stress and fatigue crack initiation and early propagation from micromechanical notches. Some attempts were made to relate the

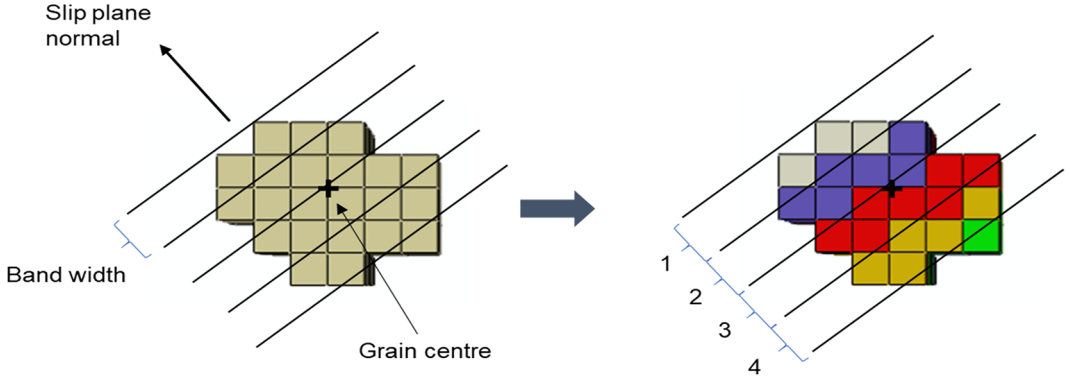

Fig. 15. Schematic illustration of assigning elements to a slip band inside the grain.

critical distance with the material grain structure and loading magnitude [49], but the lack of physical explanations reduced the method to a very effective experimental result fitting. Moreover, these approaches are empirical and cannot be used confidently to predict the fatigue lives outside the experimental domain used for calibration (e.g., different strain ranges, R-ratios, materials, notch shape, etc).

Crystal plasticity approaches can overcome the shortcomings of the theory of critical distances by explicitly modelling the microstructure effects on the early transgranular crack formation, propagation, and their variability. However, the specific skills required to implement, calibrate and compute crystal plasticity models hinder their widespread adoption in engineering applications. The novel analytical prediction method is an attempt to foster the use of crystal plasticity as industrial tool for durability and damage tolerance assessment of microstructural-size notches and manufacturing induced defect. Indeed, Equation (22) relies on a single crystal plasticity database to identify the contribution from the microstructure coupled with simpler elasto-plastic models. Additional work can further simplify the analysis by estimating k_1 and k_2 from theoretical calculations, thus avoiding the need from elastic-plastic simulations.

We also highlight that aerospace applications make widespread use of components cladded with commercially pure aluminium to enhance corrosion resistance. Prior research [34] has demonstrate that, given the low strength of pure Al, it is more common to find shallow defects and fatigue cracks on pure Al cladding compared to high strength Al alloys. Hence, our evaluation of pure Al is not only interesting for a scientific perspective, but it has direct industry impact. Moreover, the crystal plasticity model has been parameterized for the pure Al, but the results apply to a family of FCC metals with similar deformation mechanisms [50]. For example, Al 6XXX series and Stainless Steel 316 develop similar dislocation structures as pure Al and the model is likely applicable by updating the thermal stress (s_0^t), as we have shown for monotonic loading [37,51].

Finally, we note that damage tolerance performance of engineering structures containing scribe marks could be evaluated with the proposed approach, considering short crack behavior and the material intrinsic microstructural variability. We envision that planning for structure inspection and maintenance could be enhanced by the application of such analytical prognosing crystal plasticity-informed approaches along with an integrated computational-experimental validation and certification campaign. Furthermore, interactions among multiple cracks or intermetallic particles (e.g., [52]) should also be integrated into the model to further advance the prognosis of fatigue lives in notched airframe components. These approaches can further be standardized to incorporate the prognosis of fatigue damage from microstrurally small cracks.

7. Conclusions

Microstructural variability has a dominant role on early fatigue life and brings a formidable challenge engineering life prognosis. Much research on crystal plasticity has demonstrated that microstructure-sensitive models can aid in prognosis, but the computational burden of engineering component models is often impractical. Hence, this work introduced a crystal-plasticity-informed analytical formulation (Equation (22)) that quantifies the fatigue life variability induced by the microstructure at notches. This formulation is parameterized only once with a single set of crystal plasticity simulations of RVEs, which reduces the computational burden of fatigue prognosis.

The novel approach is based on band-average FIPs and relies on:

- Decoupling strain gradients induced by the microstructure and geometric strain concentrations,
- Characterizing microstructural variability once with RVEs simulations and upscaling to different notches.
- Proposing a novel vectorial FIP ($\overrightarrow{FIP}_{meso}$) that accounts multiple slip system activation,

After constructing a database with RVE simulations, the analytical approach reduces the computational time more than a factor of ten compared to crystal plasticity simulations that explicitly describe the morphology of notches. Furthermore, the comparison with experiments demonstrates that the model can capture microstructural-size notch effects to become an engineering-friendly prognosis tool.

Declaration of Competing Interest

The authors declare that they have no known competing financial interests or personal relationships that could have appeared to influence the work reported in this paper.

Acknowledgments

The authors are grateful for the support of The Punjab Educational Endowment Fund (PEEF) for funding the project.

Appendix A:. Creating slip bands in each grain

The slip bands are identified in each grain following the procedure mentioned below,
Since the FCCs have four slip planes, each element was assigned four different bands inside a grain. The elements are assigned to each band as,

- First, the centroid of the grain is determined as shown by the plus sign in Fig. 15.
- The grain is rotated along normal slip direction using the rotation matrix, and sets of planes (black lines in Fig. 15) perpendicular to slip normal plane directions are created. The distance between these planes is one bandwidth, which is the size of an element in one dimension due to homogeneity. Bands with less than one element spacing tend to be discontinuous and may have disconnected elements.
- Now, the elements are assigned to the respective bands according to their centroids position between two planes, then named as shown in Fig. 15 on the right side.
- In the schematic shown below, five planes were created inside a grain perpendicular to slip normal direction. The number assigned to a band formed by planes is called layer number and is shown with unique color below. For example, layer five is shown by a green band. Finally, GLP abbreviation is used in code to identify a particular band with its plane and grain, where G is the grain number, L is the layer number, and P is the plane number.

Appendix B

One aspect that requires consideration is the uncertainty quantification related to higher-order terms of the geometric gradient with ΔCTD_{th} in Equation (18), which were ignored to make analytical integration easier. The uncertainty was estimated by evaluating the crack growth rate with or

without a higher-order term corresponding to applied strains listed in Table 2. Fig. 16 shows that higher-order terms with ΔCTD_{th} did not contribute much towards the results, therefore ignoring these terms to make analytical integration simpler can be justified.

References

[1] Cini A, Irving PE. Development of fatigue cracks from mechanically machined scratches on 2024–T351 aluminium alloy—part I: experimentation and fractographic analysis. Fatigue Fract Eng Mater Struct 2017;40(5):776–89. https://doi.org/10.1111/ffe.12544.

[2] Khan MK. Scribe Marks at Fuselage Joints- Determination of Residual Stress and Effects of Fatigue Loading using Nanoindentation and Synchrotron X-ray Diffraction. The Open University, 2010.

[3] Nader NA. The effect of scratches on fatigue life and fatigue crack growth of Al 2024–T3 clad. Wichita State University; 1993.

[4] FAA Airworthiness Directives No. FAA-2005-20918. n.d.

[5] Das G, Kosai M, Miller M. Development of a method for damage tolerance analysis for scribe marks adjacent to fuselage longitudinal and circumferential splices. International Committee on Aeronautical Fatigue (ICAF) meeting, Napoli, Italy: 2007, p. 14–8.

[6] Inchekel A, Talia JE. Effect of scratches on the fatigue behaviour of an Al-Li alloy. Fatigue Fract Eng Mater Struct 1994;17:501–7.

[7] Talia M, Talia J. The effects of scratches and shot peening on the high cycle fatigue crack growth of aluminum alloy 2024-T3. High Cycle Fatigue of Structural Materials, Indianapolis Indiana USA: 1994, p. 409–26.

[8] Cini A, Irving PE. Development of fatigue cracks from mechanically machined scratches on 2024–T351 aluminium alloy—Part II: finite element analysis and prediction method. Fatigue Fract Eng Mater Struct 2017;40(6):853–68. https://doi.org/10.1111/ffe.12545.

[9] D. Taylor. Fatigue short cracks: the limitations of fracture mechanics. . In: K. J. Miller, E. R. de los Rios, editors. The behaviour of short fatigue cracks, London: Mechanical Engineering Publications; 1986, p. 479–90.

[10] Ritchie RO, Suresh S. The fracture mechanics similitude concept: questions concerning its application to the behavior of short fatigue cracks. Materials Science and Engineering 1983;57(2):L27–30. https://doi.org/10.1016/0025-5416(83)90223-9.

[11] McDowell DL. Basic issues in the mechanics of high cycle metal fatigue. Int J Fract 1996;80(2-3):103–45. https://doi.org/10.1007/BF00012666.

[12] Bennett V, Mcdowell D. Polycrystal orientation distribution effects on microslip in high cycle fatigue. Int J Fatigue 2003;25(1):27–39. https://doi.org/10.1016/S0142-1123(02)00057-9.

[13] Fatemi A, Socie DF. a Critical Plane Approach To Multiaxial Fatigue Damage Including Out-of-Phase Loading. Fatigue Fract Eng Mater Struct 1988;11(3):149–65. https://doi.org/10.1111/j.1460-2695.1988.tb01169.x.

[14] Suresh S. Fatigue of Materials. 2nd ed. Cambridge University Press; 1998. 10.1017/cbo9780511806575.

[15] Socie DF, Marquis GB. Multiaxial Fatigue. SAE International 1999.

[16] Sangid MD, Maier HJ, Sehitoglu H. An energy-based microstructure model to account for fatigue scatter in polycrystals. J Mech Phys Solids 2011;59(3):595–609. https://doi.org/10.1016/j.jmps.2010.12.014.

[17] Chen B, Jiang J, Dunne FPE. Is stored energy density the primary meso-scale mechanistic driver for fatigue crack nucleation? Int J Plast 2018;101:213–29. https://doi.org/10.1016/J.IJPLAS.2017.11.005.

[18] Hochhalter JD, Littlewood DJ, Veilleux MG, Bozek JE, Maniatty AM, Rollett AD, et al. A geometric approach to modeling microstructurally small fatigue crack formation: III. Development of a semi-empirical model for nucleation. Modelling Simul Mater Sci Eng 2011;19(3):035008. https://doi.org/10.1088/0965-0393/19/3/035008.

[19] Rovinelli A, Guilhem Y, Proudhon H, Lebensohn RA, Ludwig W, Sangid MD. Assessing reliability of fatigue indicator parameters for small crack growth via a probabilistic framework. Modelling Simul Mater Sci Eng 2017;25(4):045010. https://doi.org/10.1088/1361-651X/aa6c45.

[20] Castelluccio GM, McDowell DL. Mesoscale cyclic crystal plasticity with dislocation substructures. Int J Plast 2017;98:1–26. https://doi.org/10.1016/j.ijplas.2017.06.002.

[21] Patra A, McDowell DL. Crystal plasticity-based constitutive modelling of irradiated bcc structures. Phil Mag 2012;92(7):861–87. https://doi.org/10.1080/14786435.2011.634855.

[22] Bennett VP, McDowell DL. Cyclic crystal plasticity analyses of stationary, microstructurally small surface cracks in ductile single phase polycrystals. Fatigue Fract Eng Mater Struct 2002;25:677–93. https://doi.org/10.1046/j.1460-2695.2002.00530.x.

[23] Mcginty R, Mcdowell D. A semi-implicit integration scheme for rate independent finite crystal plasticity. Int J Plast 2006;22(6):996–1025. https://doi.org/10.1016/j.ijplas.2005.06.002.

[24] Castelluccio GM, Musinski WD, McDowell DL. Recent developments in assessing microstructure-sensitive early stage fatigue of polycrystals. Curr Opin Solid State Mater Sci 2014;18(4):180–7. https://doi.org/10.1016/j.cossms.2014.03.001.

[25] Castelluccio GM, McDowell DL. Mesoscale modeling of microstructurally small fatigue cracks in metallic polycrystals. Mater Sci Eng, A 2014;598:34–55. https://doi.org/10.1016/j.msea.2014.01.015.

[26] Zirkle T, McDowell DL. Analysis of monotonic and cyclic crack tip plasticity for a stationary crack tip in a FCC crystal. Comput Mater Sci 2022;202:110954.

[27] Owolabi GM, Prasannavenkatesan R, McDowell DL. Probabilistic framework for a microstructure-sensitive fatigue notch factor. Int J Fatigue 2010;32(8):1378–88. https://doi.org/10.1016/j.ijfatigue.2010.02.003.

[28] Owolabi G, Egboiyi B, Shi Li, Whitworth H. Microstructure-dependent fatigue damage process zone and notch sensitivity index. Int J Fract 2011;170(2):159–73. https://doi.org/10.1007/s10704-011-9620-z.

[29] Glinka G, Newport A. Universal features of elastic notch-tip stress fields. Int J Fatigue 1987;9(3):143–50. https://doi.org/10.1016/0142-1123(87)90069-7.

[30] Kakandar E, Barrios A, Michler J, Maeder X, Pierron ON, Castelluccio GM. A computational and experimental comparison on the nucleation of fatigue cracks in statistical volume elements. Int J Fatigue 2020;137:105633. https://doi.org/10.1016/j.ijfatigue.2020.105633.

[31] Sauzay M, Kubin LP. Scaling laws for dislocation microstructures in monotonic and cyclic deformation of fcc metals. Prog Mater Sci 2011;56(6):725–84. https://doi.org/10.1016/j.pmatsci.2011.01.006.

[32] Mura R, Ting TCT. Micromechanics of Defects in Solids. J Appl Mech 1989;56:487–8. https://doi.org/10.1115/1.3176116.

[33] Armstrong RW, Rodriguez P. Flow stress/strain rate/grain size coupling for fcc nanopolycrystals. Phil Mag 2006;86(36):5787–96. https://doi.org/10.1080/14786430600764872.

[34] Cini A. Scribe marks at fuselage joints: initiation and propagation of fatigue cracks from mechanical defects in aluminium alloys (PhD Thesis). Cranfield University, 2012.

[35] Groeber MA, Jackson MA. DREAM.3D: A Digital Representation Environment for the Analysis of Microstructure in 3D. Integrating Materials and Manufacturing Innovation 2014;3(1):56–72. https://doi.org/10.1186/2193-9772-3-5.

[36] Salahouelhadj A, Haddadi H. Estimation of the size of the RVE for isotropic copper polycrystals by using elastic–plastic finite element homogenisation. Comput Mater Sci 2010;48(3):447–55. https://doi.org/10.1016/j.commatsci.2009.12.014.

[37] Dindarlou S, Castelluccio GM. Substructure-sensitive crystal plasticity with material-invariant parameters. Int J Plast 2022;155:103306. https://doi.org/10.1016/j.ijplas.2022.103306.

[38] Castelluccio GM, McDowell DL. A mesoscale approach for growth of 3D microstructurally small fatigue cracks in polycrystals. Int J Damage Mech 2014;23(6):791–818. https://doi.org/10.1177/1056789513513916.

[39] El-Madhoun Y, Mohamed A, Bassim MN. Cyclic stress-strain response and dislocation structures in polycrystalline aluminum. Mater Sci Eng, A 2003;359(1-2):220–7. https://doi.org/10.1016/S0921-5093(03)00347-2.

[40] Risbet M, Feaugas X. Some comments about fatigue crack initiation in relation to cyclic slip irreversibility. Eng Fract Mech 2008;75(11):3511–9. https://doi.org/10.1016/j.engfracmech.2007.04.014.

[41] Yuan H, Zhang W, Castelluccio GM, Kim J, Liu Y. Microstructure-sensitive estimation of small fatigue crack growth in bridge steel welds. Int J Fatigue 2018;112:183–97. https://doi.org/10.1016/j.ijfatigue.2018.03.015.

[42] Tanaka K, Akiniwa Y. Propagation and Non-propagation of Small Fatigue Cracks. Proceedings of The 7th International Conference On Fracture (ICF7), vol. 2, Houston, Texas,: 1989, p. 869–87. https://doi.org/10.1016/b978-0-08-034341-9.50100-5.

[43] Grosskreutz JC. Fatigue Crack Propagation in Aluminum Single Crystals. J Appl Phys 1962;33(5):1787–92. https://doi.org/10.1063/1.1728832.

[44] Filippi S, Lazzarin P, Tovo R. Developments of some explicit formulas useful to describe elastic stress fields ahead of notches in plates. Int J Solids Struct 2002;39(17):4543–65. https://doi.org/10.1016/S0020-7683(02)00342-6.

[45] Castelluccio GM. A study on the influence of microstructure on small fatigue cracks. PhD. Georgia Institute of Technology, 2012.

[46] McDowell DL, Gall K, Horstemeyer MF, Fan J. Microstructure-based fatigue modeling of cast A356–T6 alloy. Eng Fract Mech 2003;70(1):49–80. https://doi.org/10.1016/S0013-7944(02)00021-8.

[47] Castelluccio GM, McDowell DL. Assessment of small fatigue crack growth driving forces in single crystals with and without slip bands. Int J Fract 2012;176(1):49–64. https://doi.org/10.1007/s10704-012-9726-y.

[48] Lucarini S, Segurado J. An upscaling approach for micromechanics based fatigue: from RVEs to specimens and component life prediction. Int J Fract 2020;223(1-2):93–108. https://doi.org/10.1007/s10704-019-00406-5.

[49] Taylor D. The Theory of Critical Distances. 1st Edition. Elsevier Science; 2007.

[50] Ashraf F, Castelluccio GM. On the similitude relation for dislocation wall thickness under cyclic deformation. Mater Sci Eng, A 2022;840:142972. https://doi.org/10.1016/j.msea.2022.142972.

[51] Ashraf F, Castelluccio GM. A robust approach to parameterize dislocation glide energy barriers in FCC metals and alloys. J Mater Sci 2021;56(29):16491–509. https://doi.org/10.1007/s10853-021-06376-1.

[52] Clark BC, Castelluccio GM, Reiterer MW, McDowell DL, Neu RW. Microstructure-sensitive fatigue modelling of medical-grade fine wire. Fatigue Fract Eng Mater Struct 2019;42(1):152–65.

2022-06-17

Analytical fatigue life formulation for notches informed by crystal plasticity

Ashraf, Farhan

Elsevier

Ashraf F, Cini A, Castelluccio GM. (2022) Analytical fatigue life formulation for notches informed by crystal plasticity, International Journal of Fatigue, Volume 163, October 2022, Article number 107072
https://doi.org/10.1016/j.ijfatigue.2022.107072